

Phase transformations in MgTbNd alloy

Bohumil Smola*, Ivana Stulíková**, Jaroslava Černá, Jakub Čížek, and Martin Vlach

Faculty of Mathematics and Physics, Charles University, Ke Karlovu 3, 121 16 Praha 2, Czech Republic

Received 20 May 2011, revised 6 July 2011, accepted 11 July 2011

Published online 15 August 2011

Keywords calorimetry, positron spectroscopy, rare earth alloys and compounds, TEM

* Corresponding author: e-mail bohumil.smola@mff.cuni.cz, Phone: +420 221 911 355, Fax: +420 221 911 1618

** e-mail ivana.stulikova@mff.cuni.cz, Phone: +420 221 911 371, Fax: +420 221 911 371

Precipitation in the MgTbNd alloy with ~4 wt.%Tb and ~2 wt.%Nd solution treated at 500 °C/4 h was studied by means of differential scanning calorimetry (DSC) with linear heating rates 1–20 K/min. Electrical resistivity measurements at 78 K, positron annihilation spectroscopy (PAS), and transmission electron microscopy (TEM) were performed on the specimens isochronally annealed in steps 20 K/20 min or 30 K/30 min. Microhardness HV0.1 annealing curves for various isochronal heating programs corresponding to linear heating rates 0.5–10 K/min revealed hardening caused by individual precipitation

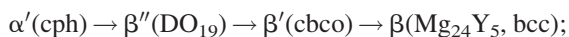
processes. The precipitation sequence includes successively DO₁₉ clusters, DO₁₉ particles, extremely small particles of the cbco phase, β₁ phase with fcc structure, β phase of Mg₅(Tb,Nd) type, and β phase of Mg₄₁(Tb,Nd)₅ type. All the particles except the last one have a plate-shape oriented in the Mg matrix in a triangular arrangement. Activation energies of the individual precipitation processes were determined from calorimetric measurements. The results of the PAS and electrical measurements correspond well to the DSC results as well as to the hardening caused by the β₁ phase particles.

© 2011 WILEY-VCH Verlag GmbH & Co. KGaA, Weinheim

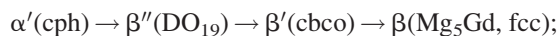
1 Introduction Magnesium alloyed with rare earth has legitimately attained attraction in last decades recognizing its potential as precipitation hardenable light alloys usable in transport, IT, or leisure industries (*e.g.*, [1]). Mg alloys have also been recently intensively investigated as a biodegradable material suitable for degradable orthopedic implants or degradable stents (*e.g.*, [2, 3]). Plate-shaped particles of transient or equilibrium phases oriented in the Mg matrix are often key constituents in Mg alloys precipitation strengthening [4, 5]. Precipitate plates formed on prismatic planes of the matrix in a dense triangular arrangement provide the most effective barriers to the motion of basal dislocations. Shear resistant small disks or plates parallel to the Mg-matrix basal planes are the weakest obstacles to the motion of basal dislocations but are strong enough to inhibit cross slip of basal dislocations and non-basal slip [4, 6].

Supersaturated rare earth (yttrium included) solid solutions in binary alloys decompose basically in three different precipitation sequences [7], namely:

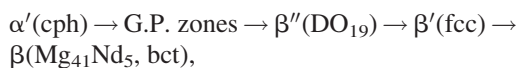
(i) Mg–Y type [8]: (Y, Tb, Dy, Ho, Er, Tm, Lu)



(ii) Mg–Gd type [9]: (Gd)



(iii) Mg–Nd type [8]: (Ce, Nd)



cph: close packed hexagonal, cbco: c-base centered orthorhombic, bcc: body centered cubic, fcc: face centered cubic, bct: body centered tetragonal structures.

These sequences may be modified in more complex Mg alloys [10–12]. Precipitation generally does not combine two independent sequences when two rare earth elements with two different precipitation sequences are alloyed, but it conforms to one of them or to the third one. Typical examples are the commercial alloy WE (Mg–Y–Nd) or Mg–Dy–Nd and Mg–Gd–Nd alloys decomposing as the Mg–Gd system. More recently, fourth intermediate precipitate, designated β₁ [11], has been observed forming between the β' and β phases in Mg–Y–Nd, Mg–Dy–Nd and Mg–Gd–Nd alloys [11, 13, 14]. Precipitates of transient phases are usually the most important in age hardening of Mg–rare earth alloys as

distributions of finer plates in a higher number density than for the equilibrium phase can be developed. Unfortunately, thermodynamic assessment is predominantly available for equilibrium phases of the Mg-rare earth systems only (e.g., [15–18]) and only little information can be found about activation energy of transient phases precipitation in Mg-rare earth alloys (e.g., [13, 19, 20]).

The present work attempts to describe the precipitation of transient and equilibrium phases in the MgTbNd alloy using differential scanning calorimetry (DSC), electrical resistivity measurements at 78 K, microhardness measurements, positron annihilation spectroscopy (PAS), transmission electron microscopy (TEM), and electron diffraction (ED).

2 Experimental details The MgTbNd alloy was prepared by squeeze casting under the protective gas atmosphere (Ar + 1%SF₆) in several ingots. The average of chemical analyses is shown in Table 1.

Solution heat treatment 500 °C/4 h finished by water quench was determined by electrical resistivity measurement. The final mean grain size increased to more than 400 μm.

The isochronal annealing responses of the relative electrical resistivity changes, microhardness and positron annihilation were measured over the range of 20–500 °C in the solution treated specimens. Annealing was carried out in steps of 20 K/20 min or 30 K/30 min and was followed by quenching. Heat treatment was performed in a stirred oil bath up to 240 °C or in a furnace with the argon protective atmosphere at higher temperatures. Relative electrical resistivity changes $\Delta\rho/\rho_0$ were obtained to an accuracy of 10⁻⁴. The resistivity was measured using the dc four-point method with a dummy specimen in series. The influence of parasitic thermo-electromotive force was suppressed by current reversal. The thermal stability of mechanical properties during the heat treatment was measured by Vickers microhardness HV0.1 at room temperature and positron lifetime (LT) or *S* parameter was measured at room temperature, too. Isochronal annealing procedures with steps of 20 K/40 min, 20 K/20 min, 20 K/10 min, 20 K/4 min, and 20 K/2 min corresponding to effective heating rates 0.5–10 K/min were used for PAS and microhardness measurements.

PAS investigations were performed using the two techniques: LT spectroscopy and measurement of Doppler

broadening (DB) of annihilation radiation. Using LT spectroscopy one can determine lifetime of positrons annihilating in various states, e.g., free positrons delocalized in lattice or positrons trapped at various open-volume defects like vacancies, vacancy clusters, dislocations, etc. [21]. Hence, LT spectroscopy enables to identify defects in the studied specimen and to determine defect densities. LT investigations were performed using a fast-fast LT spectrometer [22] with the time resolution of 150 ps (FWHM ²²Na). At least 10⁷ annihilation events were accumulated in each LT spectrum. Decomposition of LT spectra was performed using a maximum likelihood based procedure [23]. ²²Na₂CO₃ with the activity of ~1 MBq deposited on 2 μm thick Mylar foil was used as a positron source. The positron source was always sealed between two identical pieces of the measured sample. The source contribution representing the positrons annihilated in the ²²Na₂CO₃ spot and the covering Mylar foil consisted of two weak components with lifetimes of 368 ps and 1.5 ns corresponding to relative intensities of 8 and 1%.

Non-zero momentum of an annihilating electron-positron pair leads to a Doppler shift in annihilation radiation energy which is directly proportional to the momentum component into the direction of the emitted photon [24]. Doppler shift carries information about one-dimensional momentum distribution of electrons which annihilated positrons, since the momentum of the thermalized positron is negligible compared to that of an electron. Doppler shift can be either positive or negative depending on the moving direction of an annihilating pair with respect to the direction of the emitted photon and causes, thereby, a broadening of the annihilation photo-peak in the γ-ray energy spectrum. A high purity Ge detector Canberra GC3018 with the relative efficiency of 30% and energy resolution of 1.8 keV was employed for DB measurements. Signals from HPGe detector were processed in a spectroscopy amplifier Canberra 2020 and digitized in analog-to-digital converter Canberra 8713. DB measurements were performed with the same positron source as LT investigations. A precise quantification of DB was performed using so called *S* parameter defined as the central area of the annihilation peak (with subtracted background) divided by the net peak area. Hence, *S* parameter is a measure of the contribution of the positrons annihilated by low-momentum electrons. When a positron is trapped at an open volume defect its wave function becomes localized in defect which leads to a reduction in the overlap of the positron wave function with high momentum core electrons localized in atomic orbitals. Consequently, *S* increases. Hence, *S* parameter is a measure of open volume defects' concentration. DB spectroscopy provides an integral value of the *S* parameter and cannot distinguish between various positron states. However, the main advantage of DB spectroscopy is that it is substantially faster than LT measurement. Using 1.5 MBq positron source LT measurement takes typically 2 days, while DB spectrum with sufficient statistics can be accumulated within several hours.

Table 1 Composition of the investigated alloy.

| (wt.%) | | Tb | Nd | Mg | | |
|-------------------|-------|-----------|-----------|---------|-------|--------|
| | | 3.6 ± 0.4 | 2.1 ± 0.4 | balance | | |
| impurities (wt.%) | | | | | | |
| Mn | Fe | Zn | Al | Si | Cu | Ni |
| 0.014 | 0.020 | 0.001 | 0.008 | 0.009 | 0.003 | 0.0004 |

DSC curves were measured at various heating rates from 1 to 20 K/min using the Netsch DSC 200 F3 apparatus with Al_2O_3 pans at specimens previously solution heat treated. Measurements were performed with a pure Mg reference specimen and some experiments were done without a reference for a comparison. Nitrogen flowed with the rate of 40 mL/min as a protective atmosphere. TEM and ED were carried out to determine the microstructure of the alloy after specified treatments. An analysis of the phases precipitated out was also supported by energy-dispersive X-ray microanalysis. Studies of the microstructure were undertaken on the JEOL JEM 2000FX electron microscope equipped with the LINK AN 1000 micro analyzer. The specimens for TEM were prepared by the same isochronal annealing procedure as those for electrical resistivity, microhardness, and PAS measurements.

3 Experimental results The resistivity response of the solution treated MgTbNd alloy measured at 78 K on isochronal annealing 30 K/30 min up to 480 °C is shown in Fig. 1. Resistivity already diminishes after annealing at elevated temperatures. This decrease continues up to annealing temperature of 330 °C delayed only in the temperature range of 180–210 °C. The subsequent resistivity increase has no simple form and resistivity does not yet attain the initial value of the solution treated specimen after successive annealing up to 480 °C. Negative numerical derivative of the resistivity response is added in the Fig. 1.

Local maxima of the negative numerical derivative correspond to local maxima of the microhardness isochronal annealing curve with the same effective annealing rate 1 K/min – Fig. 2a. Processes causing the two-stage resistivity decrease due to annealing between 210 and 330 °C lead exceptionally to only one wider microhardness increase response within this temperature range. The microhardness value at the end of the isochronal annealing at 500 °C is lower

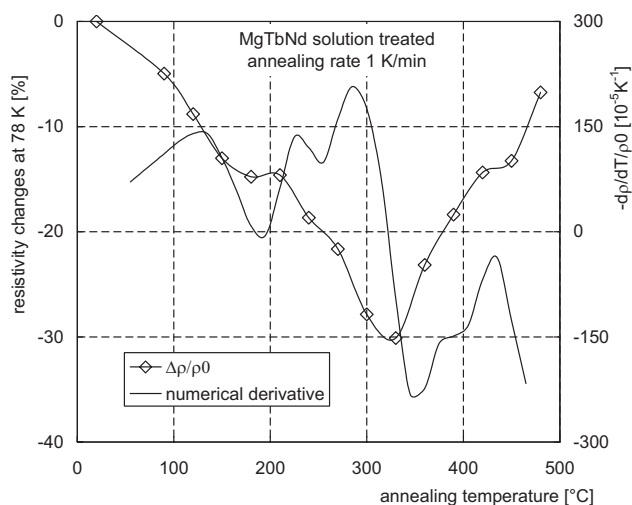


Figure 1 Relative resistivity isochronal annealing curve measured at 78 K in MgTbNd specimen solution treated 500 °C/4 h. Negative numerical derivative of the measured curve is also seen.

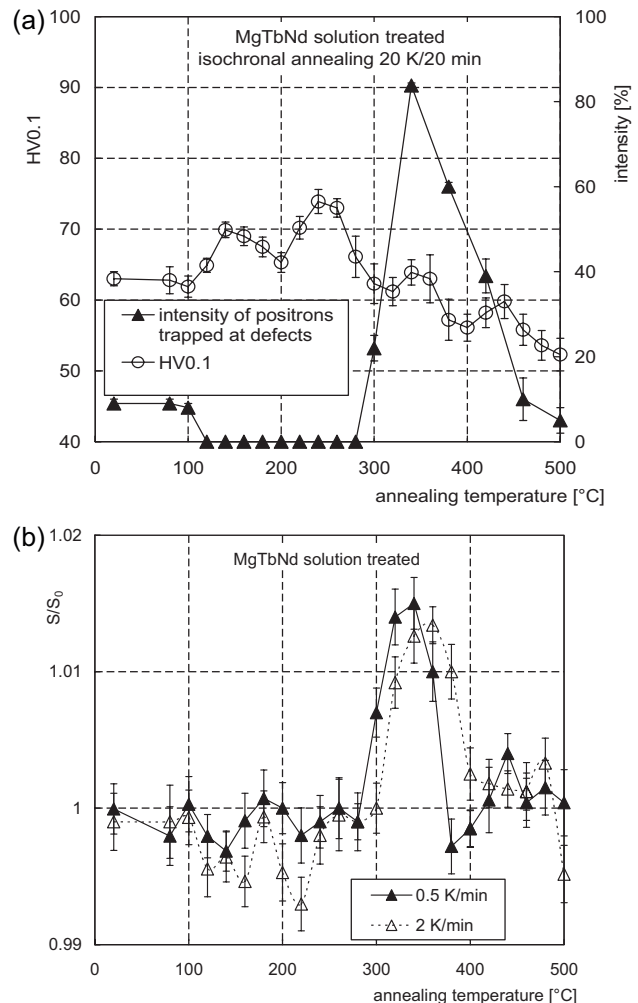


Figure 2 (a) Dependencies of microhardness HV0.1 and intensity of positrons in MgTbNd solution treated alloy on annealing temperature: complexes of quenched-in vacancies and solute atoms (below 120 °C) and misfit defects at precipitate–matrix interfaces (above 280 °C) trap positrons. Isochronal annealing program 20 K/20 min was used. (b) Temperature dependence of the S parameter measured by PAS on the specimen subjected to isochronal annealing 20 K/40 min and 20 K/10 min (effective heating rate of 0.5 and 2 K/min). All S parameters were normalized to the S parameter S_0 measured at the solution treated specimen.

than that in the solution treated condition. It corresponds well to the resistivity measurements and documents that the solid solution is not yet fully restored. LT spectra measured at the MgTbNd alloy subjected to isochronal annealing 20 K/20 min (*i.e.*, effective heating rate 1 K/min) consist of (i) a short-lived component with lifetime ≤ 230 ps representing a contribution of positrons annihilated from the free state, *i.e.*, not trapped at defects, and (ii) a long-lived component ~ 280 ps which comes from positrons trapped at defects. Single life time of 225 ps was measured in well annealed Mg [25]. The long-lived component value (280 ± 20) ps associated with positron vacancy interaction in MgTbNd alloy was

found in Ref. [26]. The long-lived component of intensity $\sim 10\%$ in the solution treated MgTbNd alloy can be attributed to positrons trapped at quenched-in vacancies bound to Tb or Nd solute atoms [25, 26]. Relative intensity of the long-lived component is plotted in Fig. 2a as a function of the annealing temperature. This component disappeared in the sample annealed at 120°C (see Fig. 2a) because the complexes of quenched-in vacancies with solute atoms are annealed out. In the temperature interval of $120\text{--}280^\circ\text{C}$ virtually all positrons in the sample annihilate from the free state, *i.e.*, the intensity of trapped positrons is zero. Another defect component with lifetime of $\sim 256\text{ ps}$ starts to rise on annealing above 280°C with the intensity maximum after annealing at 340°C – Fig. 2a. This component represents a contribution of positrons trapped in open volumes at misfit defects at the precipitate-matrix interfaces [26]. Thus, presence of this component testifies that precipitates developed in this temperature range are semi-coherent or incoherent.

DB measurements were performed on the MgTbNd alloy subjected to isochronal annealing with the effective heating rate of 0.5 K/min (steps $20\text{ K}/40\text{ min}$) and 2 K/min (steps $20\text{ K}/10\text{ min}$). Temperature dependence of the S parameter normalized to the value S_0 measured in the solution treated sample is plotted in Fig. 2b. There is a strong increase in S after annealing above 280°C indicating increasing contribution of positrons trapped at defects. This is in good agreement with the rise of the defect component detected by LT and testifies the formation of semi-coherent or incoherent precipitates. Having inspected Fig. 2a and b, one can realize that the position of the maximum contribution of positrons trapped at misfit defects, *i.e.*, maximum S value or maximum intensity of defect component, is shifted to higher temperatures in the specimens annealed with higher effective heating rate.

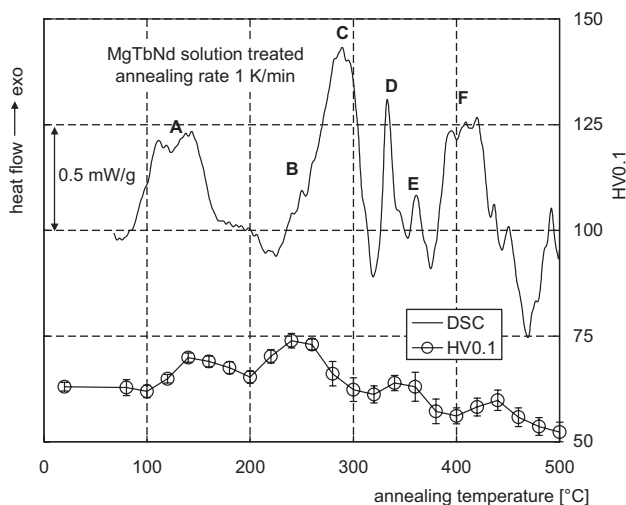


Figure 3 DSC trace in linear heating program 1 K/min of MgTbNd solution treated alloy and microhardness response to isochronal annealing $20\text{ K}/20\text{ min}$.

Up to six exothermic heat effects, marked A–F, can be distinguished in DSC curves at heating rates of $1, 5, 10,$ and 20 K/min . Figure 3 shows the DSC curve at 1 K/min together with microhardness response to isochronal annealing of $20\text{ K}/20\text{ min}$. It is seen that exothermic effects are connected with slight hardening effects. The temperature position of the heat effects shifts to higher temperatures with the increasing heating rate. The effect B is not visible at the heating rate of 1 K/min and the effect F can be distinguished only at the heating rates of 1 and 10 K/min . Only the A and D effects were detected at 20 K/min .

Local maxima of microhardness HV0.1 in isochronal annealing curves shift to higher annealing temperature, too, when isochronal annealing was performed in various annealing procedures corresponding to effective heating rates of $0.5\text{--}10\text{ K/min}$ – Fig. 4. The initial value of all solution treated specimens was the same $\text{HV}0.1 = (64 \pm 1)$, annealing curves are shifted about $\text{HV}0.1 = 10$ among each other for better separation in the Fig. 4.

The precipitation processes revealed by TEM in the MgTbNd alloy isochronally heat treated $30\text{ K}/30\text{ min}$ include subsequently all transient phases from the WE-type precipitation sequence [8, 11, 27–29]. Diffuse diffraction spots indicating the presence of very fine particles of the DO_{19} phase were observed after annealing up to 180°C – Fig. 5a. There $[22\bar{4}3]_{\alpha'-\text{Mg}}$ ED patterns overlap the $[11\bar{2}3]_{\text{DO}_{19}}$ ones – see corresponding simulated diffraction patterns in Fig. 5b. The DO_{19} phase (hexagonal ordered structure, $\text{hP}8, \text{P}6_3/\text{mmc}, a = 2a_{\text{Mg}}, c = c_{\text{Mg}}$) develops to the plates ($15\text{--}35\text{ nm}$ in diameter and $3\text{--}4\text{ nm}$ thick) parallel to all $\{11\bar{2}0\}$ planes of the α' -matrix by annealing to 240°C ; see Fig. 6 – bright field (BF) TEM image in $(1\bar{1}01)_{\alpha'-\text{Mg}}$

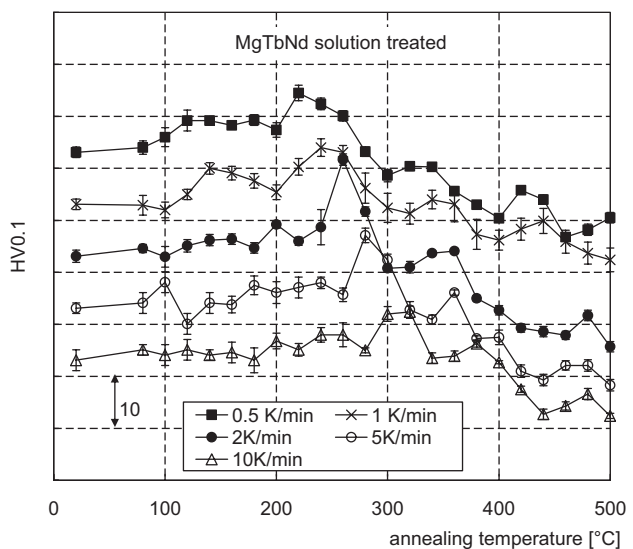


Figure 4 Isochronal annealing curves of microhardness HV0.1 measured in various isochronal annealing programs corresponding to effective heating rates of $0.5\text{--}10\text{ K/min}$. The initial value of all specimens is (64 ± 1) , annealing curves are shifted about $\text{HV}0.1 = 10$ among each other.

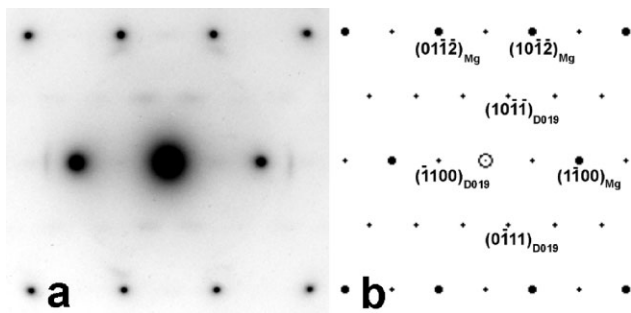


Figure 5 (a) $[22\bar{4}3]_{\alpha'-Mg}$ pole ED pattern of the MgTbNd annealed up to 180 °C with diffuse spots of $\langle 11\bar{2}3 \rangle_{DO_{19}}$ pole ED pattern. (b) Indexed simulation of ED patterns from Fig. 5a. Overlapping of $[22\bar{4}3]_{\alpha'-Mg}$ zone pattern and $[11\bar{2}3]_{DO_{19}}$ patterns.

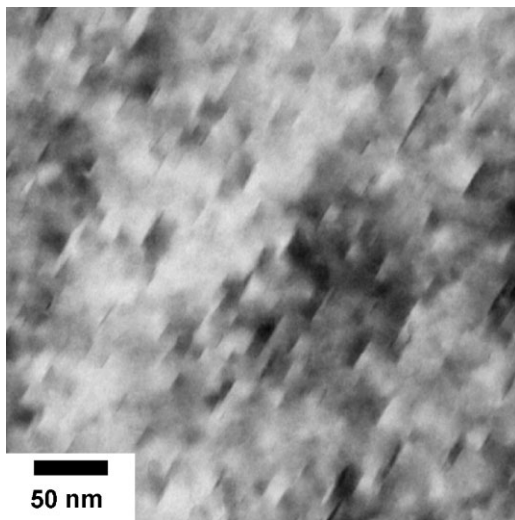


Figure 6 Plates of the DO_{19} phase parallel to $(1\bar{1}210)_{\alpha'-Mg}$ plane in MgTbNd alloy annealed up to 240 °C. BF in $(1\bar{1}01)_{\alpha'-Mg}$ reflection.

reflection. These plates persist annealing up to 270 °C without significant coarsening (the diameter 8–37 nm, the thickness 2–6 nm). However, very weak diffraction spots of the cbco phase (c base-centered orthorhombic, $a = 2a_{Mg}$, $b = 8d(1100)_{Mg}$, $c = c_{Mg}$) suggest that a low volume fraction of this phase coexists with the DO_{19} phase after isochronal annealing to 270 °C – Fig. 7a. The $[22\bar{4}3]_{DO_{19}}$, $[201]_{Cbco}$ and two $\langle 212 \rangle_{Cbco}$ pole patterns overlap there the $[44\bar{8}3]_{\alpha'-Mg}$ zone patterns – see simulation of ED patterns in Fig. 7b. The highest hardening over the whole temperature range studied results from this microstructure. The following transient β_1 phase (DO_3 fcc structure, $a \sim 0.74$ nm) forms as plates embedded at the $\{10\bar{1}0\}$ planes of the α' -matrix.

Figure 8 shows them (~ 600 nm in diameter and ~ 15 nm in thickness) developed after the isochronal anneal up to 330 °C. This phase is semi-coherent in the Mg-matrix which is confirmed by a strong rise in the intensity of positrons trapped in defects at precipitate-matrix interfaces and the S parameter – see Fig. 2a, b. The β_1 phase particles transform in situ [11] to the β phase (Mg_5Gd -type, fcc structure,

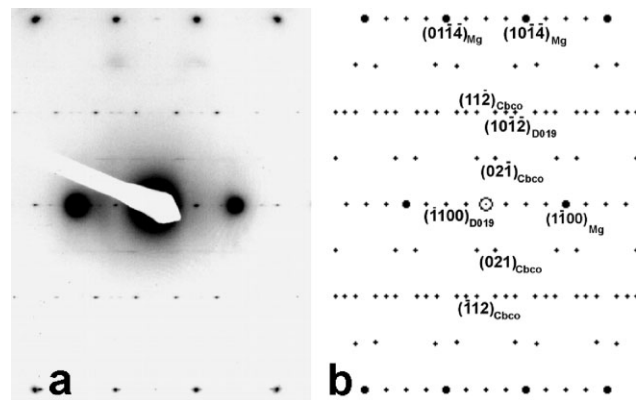


Figure 7 (a) $[22\bar{4}3]_{DO_{19}}$, $[201]_{Cbco}$, and two $\langle 212 \rangle_{Cbco}$ pole ED patterns overlap $[44\bar{8}3]_{\alpha'-Mg}$ zone patterns in the MgTbNd alloy annealed up to 270 °C. (b) Simulation of ED patterns from Fig. 7a. Overlapping of $[44\bar{8}3]_{\alpha'-Mg}$, $[22\bar{4}3]_{DO_{19}}$, $[201]_{Cbco}$, $[212]_{Cbco}$, and $[2\bar{1}2]_{Cbco}$ pole patterns.

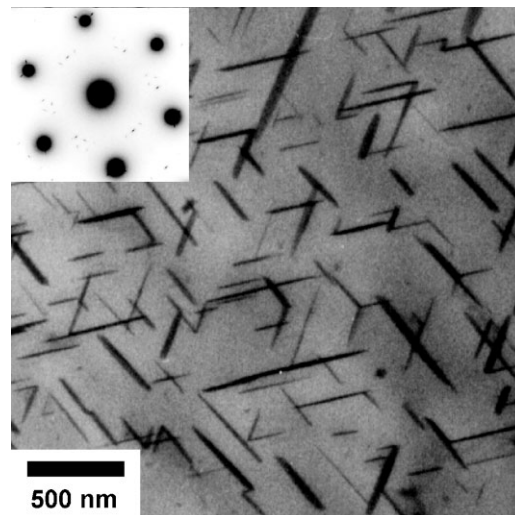


Figure 8 BF of the β_1 phase plates parallel to all $\{10\bar{1}0\}_{\alpha'-Mg}$ planes in the MgTbNd alloy annealed up to 330 °C. Corresponding $[0001]_{\alpha'-Mg}$ ED patterns in the inset.

$a = 2.23$ nm). Prismatic plates of the β phase were identified after annealing up to 390 °C in the size ~ 0.5 – 1 μm in diameter and ~ 25 nm thickness with noticeably lower number density than that of β_1 plates after annealing to 330 °C – Fig. 9. These plates were observed even after an isochronal anneal up to 450 °C with increasing thickness (~ 50 nm) but with a negligible increase in diameter.

Irregular particles of the $Mg_{41}(Tb,Nd)_5$ phase [body centered tetragonal structure $a = (1.4764 \pm 0.0004)$ nm, $c = (1.0429 \pm 0.0003)$ nm] were also rarely observed after this annealing in grain interiors – see the diffraction pattern in Fig. 10. Resistivity increases from annealing temperature 330 °C (Fig. 1) as a result of particles dissolution combined with $\beta_1 \rightarrow \beta$ transformation. As precipitates grow and their number density diminishes with annealing temperatures

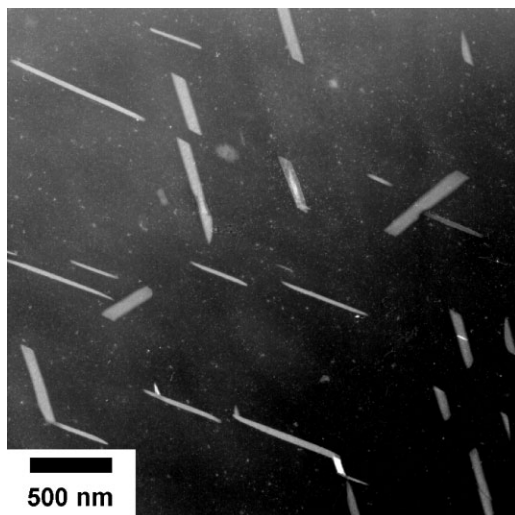


Figure 9 Plates of the β phase parallel to all $\{10\bar{1}0\}_{\alpha'-\text{Mg}}$ planes in the MgTbNd alloy annealed up to 390 °C. DF image in reflection of β phase.

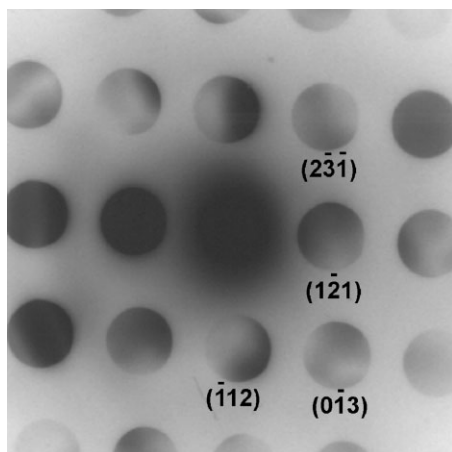


Figure 10 Microdiffraction patterns from the particle of the $\text{Mg}_{41}(\text{Tb}, \text{Nd})_5$ phase in the MgTbNd alloy annealed up to 450 °C. [531] pole of the $\text{Mg}_{41}(\text{Tb}, \text{Nd})_5$ phase.

higher than 340 °C, their interface area decreases and thereby the intensity of positrons trapped at interface defects decreases, too.

4 Discussion Comparing the results of microstructure development study and DSC measurements individual precipitation processes, namely $\alpha'(\text{cph}) \rightarrow \beta''(\text{DO}_{19} \text{ clusters}) \rightarrow \beta''(\text{DO}_{19} \text{ plates}) \rightarrow \beta'(\text{cbco}) \rightarrow \beta_1(\text{Mg}_3\text{Gd}, \text{fcc}) \rightarrow \beta(\text{Mg}_5\text{Gd}, \text{fcc}) \rightarrow \beta(\text{Mg}_{41}\text{Nd}_5, \text{bct})$ were assigned to the stages A–F. Using the Kissinger method – Fig. 11 with the assumption that the peak temperature T_m in DSC curves for individual precipitation processes can be expressed as

$$\ln(\Phi/T_m^2) = -\frac{E}{RT_m} + C, \quad (1)$$

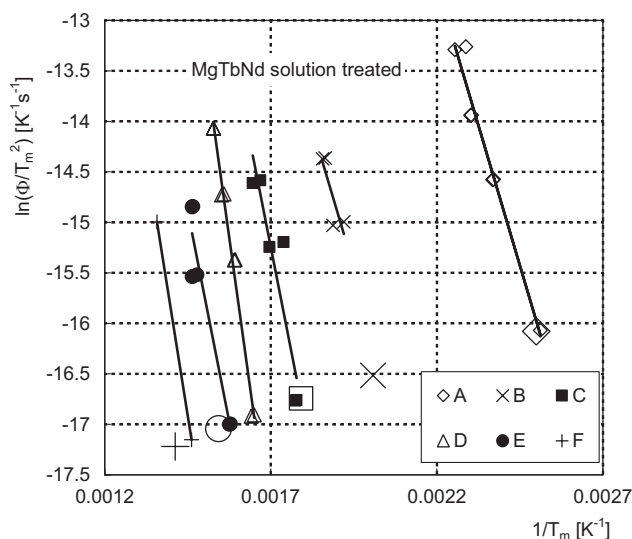


Figure 11 Kissinger plot of exothermic heat effects (precipitation: β'' DO_{19} clusters – A, β'' DO_{19} plates – B, β' cbco phase – C, β_1 fcc plates – D, β fcc plates – E, β bct phase – F) in the solution treated MgTbNd alloy. Large symbols are the results from resistivity annealing curve in the annealing program 30 K/30 min – see Fig. 1. Φ is the linear heating rate; T_m is the peak temperature of DSC trace for particular exothermic heat effect.

where C is a constant, E the activation energy of the precipitation process, R the gas constant, Φ a heating rate, and T_m is the peak temperature of the DSC signal, the values of the activation energy were determined as listed in the Table 2. Large symbols correspond to the maxima of numerical derivative of resistivity from Fig. 1, but activation energies were determined from DSC measurements only. The peak temperature for the process D is not seen in resistivity measurements due to a complex resistivity behavior in this temperature range reflecting also a solution process.

The activation energy increases with the sequential phase development up to the β_1 phase formation. The measured energy of DO_{19} cluster formation is somewhat higher than that for the GP formation in the Mg-0.5 at% Nd alloy determined by resistivity measurements [19] and than the energy of Y and Nd migration in Mg determined from serrated flow in the WE54 alloy [30] (both 75 kJ/mol). It lies within the limits of the value for the β'' formation early stage in the Mg–Nd–Gd–Zr alloy (75 ± 14) kJ/mol [20]. The precipitation energy of the next stage – DO_{19} plates corresponds to the value for the β'' formation later stage in the Mg–Nd–Gd–Zr alloy (111 ± 12) kJ/mol determined by SAXS [20]. The value of the activation energy of β_1 formation agrees with the value obtained by DSC in the WE43 alloy for the same process (183 kJ/mol [13]). The determined activation energy for β phase precipitation in the studied MgTbNd alloy is somewhat lower than that of β_1 formation in accordance with the WE43 alloy [13] and close to the Mg self-diffusion energy [31].

Table 2 Activation energies in kJ/mol of the precipitation processes in the MgTbNd alloy determined by the Kissinger method.

| β'' DO ₁₉ clusters A | β'' DO ₁₉ plates B | β' cbco phase C | β_1 fcc plates D | β fcc plates E | β bct phase F |
|---------------------------------------|-------------------------------------|-----------------------|------------------------|----------------------|---------------------|
| 92 ± 7 | 93 ± 39 | 139 ± 29 | 197 ± 10 | 139 ± 20 | 173 |

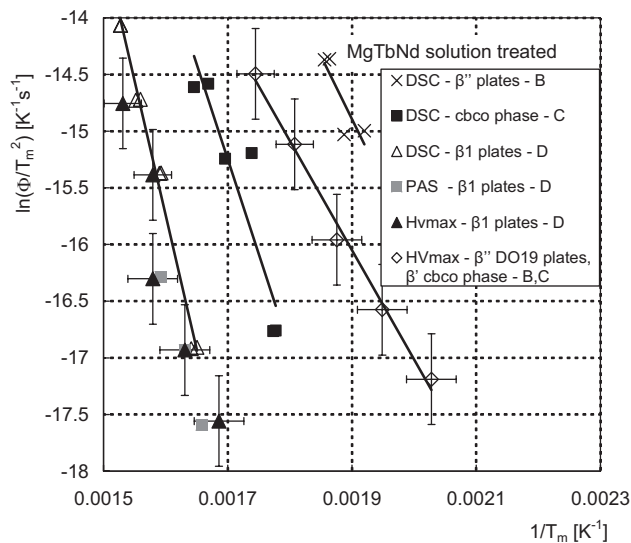


Figure 12 Kissinger plot of DSC heat effects B, C, and D (B – formation of β'' DO₁₉ plates, C – formation of β' cbco phase, D – formation of β_1 fcc plates) together with the results of PAS and HV0.1 response to β_1 phase formation – PAS–D and HVmax–D. HV0.1 response to DO₁₉ and cbco phase formation is also added – HVmax – B, C.

A comparison of PAS results (LT + DB) and HV0.1 measurements with calorimetric measurements is shown in Fig. 12. Temperatures of the peak defect component intensity (Fig. 2a) and the peak *S* parameter value (Fig. 2b) corresponding to the maximum contribution of the positrons trapped at the β_1 plates interfaces were chosen in the Kissinger plot. The DSC results for the processes B – formation of DO₁₉ plates, C – cbco phase development and D – formation of β_1 phase are redrawn from Fig. 11. The PAS results correspond very well to the heat response. Maximum hardening caused by β_1 phase particles also agrees surprisingly well with the DSC measurements, although hardening depends not only on the precipitate volume fraction but also on the particle shape and number density. It is therefore not sure, if the maximum hardening guarantees the same volume fraction precipitated. Significantly worse agreement between the microhardness response and calorimetric measurements exists for the DO₁₉ plates and the cbco phase formation. The maximum hardening occurs after annealing at temperatures lying between the DSC peak temperature of the DO₁₉ plates formation and the DSC peak temperature of the cbco phase. Co-occurrence of DO₁₉ and cbco phases observed in this temperature range (see Fig. 7) is most probably an optimum combination leading to the peak age

hardening. Although a correlation of the measured values in the Kissinger plot is relatively good, the slope gives somewhat lower activation energy than that obtained for both DO₁₉ plates and cbco phase formation from the DSC.

5 Conclusions Precipitation of transient and equilibrium phases in the MgTbNd alloy with ~4 wt.%Tb and ~2 wt.%Nd previously solution treated at 500 °C/4 h follows the sequence α' (cph) → β'' (DO₁₉ clusters) → β'' (DO₁₉ plates) → β' (cbco) → β_1 (Mg₃(Tb,Nd), fcc) → β (Mg₅(Tb,Nd), fcc) → β (Mg₄₁(Tb,Nd)₅, bct). Plates of the DO₁₉ phase and the cbco phase coexist in Mg. The β_1 phase transforms in situ to the β phase of the Mg₅(Tb,Nd) type. A coexistence of this phase and the Mg₄₁(Tb,Nd)₅ type phase was also proved. It is not possible to determine if both β phases observed are the stable ones or if only the Mg₄₁(Tb,Nd)₅ type is the equilibrium phase.

All transient phases mentioned precipitate as plates, the size of the cbco phase is extremely small. Only irregular particles of the Mg₄₁Nd₅ type phase were rarely found after the successive annealing up to 500 °C.

The activation energies obtained from the DSC data analysis using the Kissinger method increase from 92 to 197 kJ/mol for the DO₁₉ cluster formation to the development of the β_1 phase. The activation energies of both β phases formation are lower than the energy for the β_1 phase formation (139 and 173 kJ/mol).

The PAS results and HV0.1 response on β_1 phase precipitation correspond very well to the heat response.

Acknowledgements The support by the Czech Science Foundation (GACR 106/09/0407 and P108/10/0648) and by the Ministry of Education of the Czech Republic within the framework of the research program MSM 0021620834 is gratefully acknowledged.

References

- [1] B. L. Mordike and T. Ebert, *Mater. Sci. Eng. A* **302**, 37 (2001).
- [2] M. P. Staiger, A. M. Pietak, J. Huadmai, and G. Dias, *Biomaterials* **27**, 1728 (2006).
- [3] N. Hort, Y. Huang, D. Fechner, M. Störmer, C. Blawert, F. Witte, C. Vogt, H. Drücker, R. Willumeit, K. U. Kainer, and F. Feyerabend, *Acta Biomater.* **6**, 1714 (2010).
- [4] J. F. Nie, *Scr. Mater.* **48**, 1009 (2003).
- [5] B. Smola, I. Stulíková, J. Pelcová, and B. L. Mordike, *J. Alloys Compd.* **378**, 196 (2004).
- [6] B. L. Mordike, I. Stulíková, and B. Smola, *Met. Mater. Trans.* **36A**, 1729 (2005).
- [7] I. J. Polmear, *Magnesium alloys*, in: *Light Alloys*, 4th ed. (Elsevier, NY, 2005), pp. 237–297.

- [8] G. W. Lorimer, in: *Proceedings Magnesium Technology*, London, UK, 1986, Inst. of Metals, UK, pp. 47–51.
- [9] P. Vostrý, B. Smola, I. Stulíková, F. von Buch, and B. L. Mordike, *Phys. Status Solidi A* **175**, 491 (1999).
- [10] J. Kiehn, B. Smola, P. Vostrý, I. Stulíková, and K. U. Kainer, *Phys. Status Solidi A* **164**, 709 (1997).
- [11] J. F. Nie and B. C. Muddle, *Acta Mater.* **48**, 1691 (2000).
- [12] B. Smola and I. Stulíková, *J. Alloys Compd.* **381**, L1 (2004).
- [13] G. Riontino, D. Lussana, and M. Massazza, *J. Therm. Anal. Calorim.* **83**, 643 (2006).
- [14] G. Riontino, D. Lussana, M. Massazza, G. Barucca, P. Mengucci, and R. Ferragut, *J. Alloys Compd.* **463**, 200 (2008).
- [15] F. G. Meng, J. Wang, H. S. Liu, L. B. Liu, and Z. P. Jin, *Mater. Sci. Eng. A* **454/455**, 266 (2007).
- [16] O. B. Fabrichnaya, H. L. Lukas, G. Effenberg, and F. Aldinger, *Intermetallics* **11**, 1183 (2003).
- [17] J. Gröbner, A. Kozlov, R. Schmid-Fetzer, M. A. Easton, S. Zhu, M. A. Gibson, and J. F. Nie, *Acta Mater.* **59**, 613 (2011).
- [18] J. Gröbner and R. Schmid-Fetzer, *Scr. Mater.* **63**, 674 (2010).
- [19] T. J. Pike and B. Noble, *J. Less-Common Met.* **30**, 63 (1973).
- [20] R. Ferragut, F. Moia, F. Fiori, D. Lussana, and G. Riontino, *J. Alloys Compd.* **495**, 408 (2010).
- [21] P. Hautojärvi and C. Corbel, in: *Proceedings of the International School of Physics “Enrico Fermi” Course CXXV*, edited by A. Dupasquier and A. P. Mills (IOS Press, Amsterdam, 1995), pp. 491–532.
- [22] F. Bečvář, J. Čížek, L. Lešták, I. Novotný, I. Procházka, and F. Šebesta, *Nucl. Instrum. Methods A* **443**, 557 (2000).
- [23] I. Procházka, I. Novotný, and F. Bečvář, *Mater. Sci. Forum* **255–257**, 772 (1997).
- [24] P. Hautojärvi, *Introduction to positron annihilation*, in: *Positrons in Solids*, edited by P. Hautojärvi (Springer-Verlag, Berlin, 1979), pp. 1–22.
- [25] J. Čížek, I. Procházka, B. Smola, I. Stulíková, and M. Vlach, in: *Magnesium, Proc. 7th Int. Conf. on Magnesium Alloys and Their Applications*, edited by K. U. Kainer (Wiley-VCH Verlag, Weinheim, 2007), pp. 517–522.
- [26] J. Čížek, I. Procházka, B. Smola, I. Stulíková, M. Vlach, R. K. Islamgaliev, and O. Kulyasova, *Mater. Sci. Forum* **584–586**, 591 (2008).
- [27] J. F. Nie and B. C. Muddle, *Scr. Mater.* **40**, 1089 (1999).
- [28] C. Antion, P. Donnadieu, F. Perrard, A. Deschamps, C. Tassin, and A. Pisch, *Acta Mater.* **51**, 5335 (2003).
- [29] P. J. Apps, H. Karimzadeh, J. F. King, and G. W. Lorimer, *Scr. Mater.* **48**, 1023 (2003).
- [30] S. M. Zhu and J. F. Nie, *Scr. Mater.* **50**, 51 (2004).
- [31] J. Combronde and G. Brebec, *Acta Metal.* **19**, 1393 (1971).